Journal of Innovative Optical Health Sciences
Vol. 6, No. 2 (2013) 1350015 (11 pages)

DOI: 10.1142/S1793545813500156

World Scientific
www.worldscientific.com

SEGMENTATION AND CORRELATION OF OPTICAL COHERENCE TOMOGRAPHY AND X-RAY IMAGES FOR BREAST CANCER DIAGNOSTICS

JONATHAN G. SUN[*,†], STEVEN G. ADIE[*],
ERIC J. CHANEY[*] and STEPHEN A. BOPPART[*,†,‡,§]
[*]*Beckman Institute for Advanced Science and Technology*
405 North Mathews Avenue, Urbana, Illinois 61801, USA

[†]*Department of Bioengineering*
Beckman Institute for Advanced Science and Technology
405 North Mathews Avenue, Urbana, Illinois 61801, USA

[‡]*Departments of Electrical and Computer Engineering*
and Internal Medicine University of Illinois
at Urbana-Champaign, Urbana, Illinois, USA
[§]*boppart@illinois.edu*

Received 10 January 2013
Accepted 18 February 2013
Published 12 April 2013

Pre-operative X-ray mammography and intraoperative X-ray specimen radiography are routinely used to identify breast cancer pathology. Recent advances in optical coherence tomography (OCT) have enabled its use for the intraoperative assessment of surgical margins during breast cancer surgery. While each modality offers distinct contrast of normal and pathological features, there is an essential need to correlate image-based features between the two modalities to take advantage of the diagnostic capabilities of each technique. We compare OCT to X-ray images of resected human breast tissue and correlate different tissue features between modalities for future use in real-time intraoperative OCT imaging. X-ray imaging (specimen radiography) is currently used during surgical breast cancer procedures to verify tumor margins, but cannot image tissue *in situ*. OCT has the potential to solve this problem by providing intraoperative imaging of the resected specimen as well as the *in situ* tumor cavity. OCT and micro-CT (X-ray) images are automatically segmented using different computational approaches, and quantitatively compared to determine the ability of these algorithms to automatically differentiate regions of adipose tissue from tumor. Furthermore, two-dimensional (2D) and three-dimensional (3D) results are compared. These correlations, combined with real-time intraoperative OCT, have the potential to identify possible regions of tumor within breast tissue

which correlate to tumor regions identified previously on X-ray imaging (mammography or specimen radiography).

Keywords: Optical imaging; mammography; specimen radiography; segmentation; breast cancer; intraoperative imaging.

1. Introduction

Breast cancer is estimated to be the leading form of new non-skin cancer cases affecting women in the United States in 2013.[1] As medicine evolves, new treatment options have developed, with a combination of surgery, radiation therapy, chemotherapy and hormone therapy being prescribed on an individual basis.[2] However, early detection still remains a critical factor for successful treatment and increased patient survival rates.[3,4] Currently, the standard practice for screening for breast cancer includes physical examination and X-ray mammography. Suspicious lesions found on mammography are subsequently biopsied to provide specimens for pathological diagnosis, and surgical resection may follow. During surgery, resected breast masses containing tumor are frequently imaged with specimen radiography (X-rays) to help determine if the entire lesion has been resected with a sufficient margin of apparently normal tissue. Both X-ray mammography and specimen radiography rely on tissue contrast between normal and abnormal regions based on X-ray absorption and scattering. However, the introduction of other imaging modalities and tissue contrast mechanisms offers the potential to improve the diagnostic capabilities in the intraoperative setting.

Optical coherence tomography (OCT) was first described in 1991[5] and over the last two decades has been developed for applications in medicine, surgery, biology and materials testing.[6,7] OCT can noninvasively visualize optical scattering properties arising from differences in refractive index within a sample area, such as from scattering particles or boundaries. OCT is rapidly becoming an established biomedical imaging technique because it uniquely offers noninvasive micron-level resolution capable of visualizing microscopic cell and tissue features in real time up to several millimeters deep in highly-scattering tissues. Relatively inexpensive compared to many other imaging modalities, OCT systems can be portable, and interface with a variety of beam-delivery systems such as microscopes, catheters, needles or hand-held probes. Most notably in ophthalmology, OCT has become the gold-standard for retinal imaging because of the transparent nature of the eye. Ocular disease detection has advanced with the ability to look beneath the surface of the retina, as well as visualize anterior segment structures.[8–14] OCT also has applications in dentistry[15–18] and dermatology,[19–21] among many other areas.

In oncology, OCT has been used to differentiate between normal and abnormal breast tissue.[22,23] Using OCT, it has been shown that positive tumor margins on freshly excised breast masses can be accurately identified intraoperatively during breast lumpectomy procedures.[24] Furthermore, there is ongoing work involving intraoperative OCT lymph node imaging to provide real-time assessment of sentinel lymph nodes for determining tumor metastases and staging cancer.[25–27] A commercial OCT system that implements interferometric synthetic aperture microscopy (ISAM)[28] has been used for *in vivo* imaging of the tumor cavity during breast surgeries.[29] The use of other optical imaging technologies have been investigated to address the need for high-resolution assessment of tumor margins during breast cancer surgery, including elastic scattering spectroscopy,[30] Raman spectroscopy,[31] photoacoustic imaging[32] and diffuse reflectance spectroscopy,[33] among several others. While many of these have shown promise, several are hampered by factors such as point-based measurements, long acquisition times, lower spatial resolution or the generation of spectroscopic signatures, rather than image-based data. The work in this study offers the potential to correlate real-time intraoperative OCT findings with those obtained using pre-operative X-ray mammography and intraoperative specimen radiography.

2. Methods

Human breast tissue containing a portion of breast tumor (ductal carcinoma *in situ*) was obtained from

Carle Foundation Hospital, Urbana, Illinois, under a protocol approved by the Institutional Review Boards at Carle Foundation Hospital and the University of Illinois at Urbana-Champaign. Imaging of tumor specimens was performed using each modality in succession, keeping the orientation and imaging areas correlated. Specimens were first imaged with a custom-built spectral-domain OCT system that utilized a titanium:sapphire laser (KMLabs, Inc.) as an optical source. This source provided broadband light centered at 800 nm with a 100 nm bandwidth, yielding an axial resolution of 4 μm. The transverse resolution of the system was 12 μm. Following OCT imaging, specimens were either maintained in the same cuvette or transferred to a second cuvette for imaging with a commercial micro-CT (X-ray) system (MicroXCT-400, Xradia, Inc.). After imaging, specimens were either placed in formalin for paraffin-embedded histology or flash frozen for frozen section histology. Four specimens (each $\sim$ 5 mm diameter) were imaged with both OCT and micro-CT, and an additional 4 specimens used for analysis were imaged with only OCT. A total of 2400 OCT images were collected and 1250 images were analyzed. A total of 2200 micro-CT images were collected and 760 were analyzed. Subsets of images were not analyzed because they were acquired at the edges of the tissue specimens and either contained a very small portion of the tissue (low signal) or were excessively noisy (high background). The determination of which raw images were used for analysis and which were discarded was based on manual inspection of each image to ensure there was sufficient signal-to-noise to visually identify the presence of tissue in the image.

In the clinical setting, digital specimen radiography systems (Faxitron Bioptics, LLC) are often used. This portable system would typically be located immediately outside an operating room where a radiologist can provide real-time feedback on a resected tissue mass. These types of systems use X-ray energies ranging from 10−35 keV. Standard X-ray mammography scans use X-ray energies from 24−32 keV, although lower energies may be used to enhance contrast at the expense of penetration depth. The micro-CT system used in this study can image at most all of the typical X-ray energies used in both X-ray mammography and specimen radiography, with an X-ray photon energy range of 20 to 80 keV. An X-ray energy of 30 keV was used to acquire the images in this study because this closely approximated the energies used in these clinical systems. The commercial micro-CT system had a machine specification resolution capability of 200 nm, but this level of detail was not apparent in the images taken with the device. Following OCT and micro-CT imaging, specimens were histologically prepared, sectioned, stained with hematoxylin and eosin and viewed under bright field microscopy.

Three MATLAB algorithms were developed to automatically segment the acquired images, modified from community-developed algorithms from MATLAB Central.[34] The first algorithm applied an amplitude filter to an image based on a user-defined threshold (using the *im2bw* function on a grayscale image). The second algorithm, a 2D spatial frequency filter, applied a band-pass filter in the Fourier domain (using the *fft2* and *ifft2* functions) with a specified bandwidth around a center frequency, and isolated features within that range using a window function. The third algorithm applied a texture-based filter, which found entropy values (using the *entropyfilt* function as well as the *mat2gray*, *im2bw* and *bwareopen* functions) throughout a cross-sectional B-mode OCT image and made a binary decision to create a region based on similar features within a user-defined correlation distance. Each filter and segmentation approach was experimentally optimized by adjusting filter parameters to obtain a segmentation result similar to manual visual segmentation, which served as the gold-standard for comparison. This filter parameter optimization was done on a training set comprised of a total of 25 randomly selected images and a Student's *t*-test was performed to determine statistical significance. Then, for each segmentation approach, an additional algorithm was written to automatically read the images in a data set sequentially (using the *imread* function), process the images with optimum parameters and calculate an area and perimeter value for the tumor region in each image (using the *regionprops* function). Additionally, the texture-based segmentation algorithm had an additional optimization portion as it had a large variance in results from the initial training set. Two of the parameters (kernel size and correlation distance) were varied and the set with the lowest variance was used so that variability in results was minimized. Each of these algorithms was then applied to the remaining OCT and micro-CT

image data sets ($n = 1225$ for OCT and $n = 735$ for micro-CT) and the results analyzed using a Student's t-test.

3. Results and Discussion

3.1. *Manual image correlation*

For accurate correlations between different image sections of a specimen across modalities, the orientation and axes of imaging were maintained. The OCT scan volumes were generally smaller ($\sim 2\,\text{mm} \times 2\,\text{mm} \times 1.5\,\text{mm}$) compared to the micro-CT volumes ($\sim 5\,\text{mm} \times 5\,\text{mm} \times 3\,\text{mm}$) due to instrument scan parameters, and therefore the OCT volumes did not encompass the entire specimen. When comparing the two modalities, as well as comparing with corresponding histological findings (see Fig. 1), it can be seen that each modality serves a specialized role in imaging breast cancer. X-ray imaging prominently shows the presence of microcalcifications and variations in tissue density (see Fig. 1), which is not surprising, given the strong and differential X-ray attenuation by these features. OCT, in comparison, can provide morphological information based on optical scattering, and offers a different type of tissue contrast that yields different structural features. As seen in Fig. 1, suspicious microstructures visualized with OCT are not apparent in the micro-CT scan. However, because of the reduced field-of-view and imaging depth of OCT, applications are somewhat limited to specific uses where the tissue sites have been exposed, and suspicious regions have already been identified, such as in intraoperative imaging.

3D correlations can also be useful. Commercial biomedical image visualization software (Amira, Visualization Sciences Group) was used to manually co-register different morphological features. In this way, the rough orientation of the sample was obtained between modalities and features within the specimen were more easily correlated by looking at corresponding computationally extracted slices. 3D volumes of micro-CT and OCT were compared on the same scale and orientation (see Fig. 1). Although the attenuation of X-rays is not

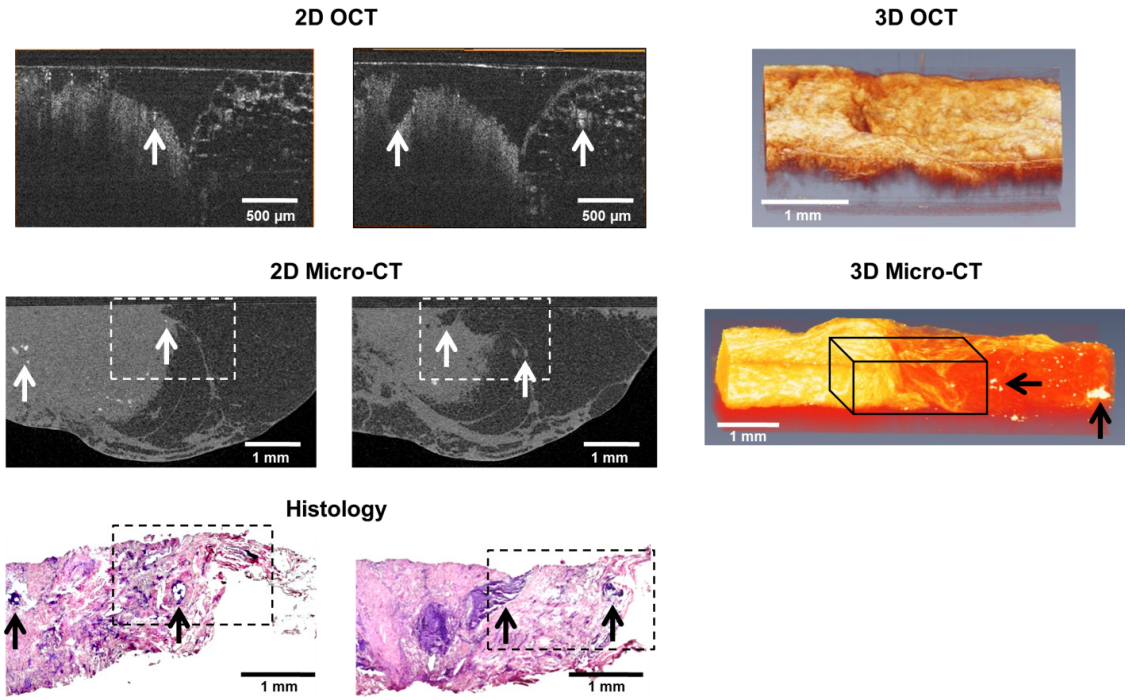

Fig. 1. Representative comparison of OCT, micro-CT and histology image data. The dotted white boxes in the micro-CT images and the dotted black boxes in the histology images (H&E) are the approximate scan areas of the corresponding OCT images. Tumor structures can be seen in all three modalities on the left-half of the images, with normal adipose tissue on the right-half. The arrows indicate corresponding structures and areas of microcalcifications. 3D OCT and micro-CT datasets are also shown. The black 3D wire-frame in the micro-CT image is the approximate scan area for the corresponding 3D OCT image. Microcalcifications (black arrows) appear bright in the micro-CT data of the adipose tissue on the right. The micro-CT volume is visualized using a direct volume rendering algorithm while the OCT volume is visualized using a surface mesh algorithm.

significantly different between fibrous tissue and cancerous tissue, three separate tissue types were readily differentiable: adipose tissue, tumor tissue and microcalcifications. Similarly, these three tissue types were readily identified with OCT (see Fig. 1). The adipose tissue had a honeycomb network texture pattern based on the higher scattering by the adipocyte cell membranes. The tumor tissue was more homogeneous and higher scattering, and the microcalcifications were point-like objects that exhibited the highest amount of optical scattering. Based on these common image features between modalities, it was possible to segment and correlate images between modalities.

3.2. *Optimizing segmentation methods*

Following alignment of the orientation, scale and fields-of-view between OCT and micro-CT data volumes, three MATLAB algorithms modified from community-developed algorithms were utilized to automatically segment images. Each algorithm made a binary decision, delineating tumor regions and areas.

The first algorithm used an intensity filter to segment out tumor areas as seen in Fig. 2 (OCT and micro-CT). For the OCT data set, threshold values were optimized to 20%, based on visually determining the value that highlighted the tumor

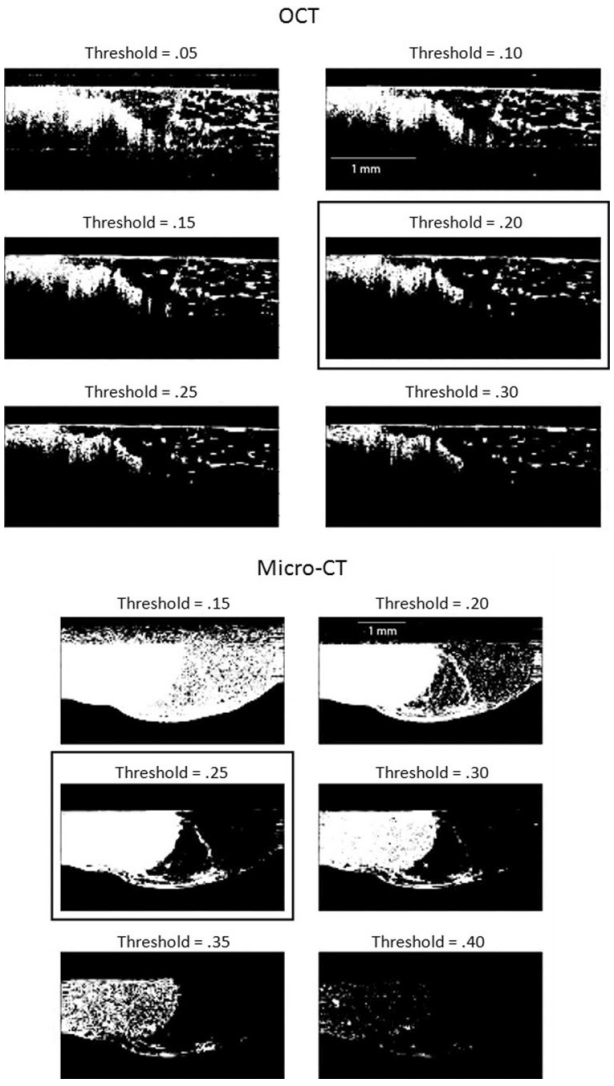

Fig. 2. Optimization of intensity-based filtering. OCT images (top set) with intensity threshold settings from 5−30% and micro-CT images (bottom set) with threshold values from 15−40% are shown. Setting threshold values at 20% for OCT and 25% of maximum intensity for micro-CT yielded the best results by visual selection (boxes). The image dimensions were 3 mm × 1.5 mm and the tumor area is shown on the left side of each image.

area best while minimizing the signal from the adipose tissue. For micro-CT, a threshold value of 25% was found to be optimal, as almost the entire tumor region was segmented without significant signal from the adipose tissue.

Intensity filtering yielded better segmentation results for micro-CT data because of the large X-ray absorption contrast between the tumor and adipose regions. In the scattering-based OCT images, there are regions of adipose tissue that are more visible due to scattering from the adipocyte cell membranes. As such, the intensity filter was not as effective for OCT image segmentation in this comparison. This intensity filter algorithm, however, was the fastest, requiring only 0.7 s per OCT image and 0.1 s per micro-CT image on a 2.93 GHz Intel quad-core personal computer.

The second algorithm for segmentation was spatial frequency filtering. This method was chosen because tumor areas are denser and have different spatial frequency content in images compared to adipose tissue. This algorithm applied a band-pass filter in the Fourier domain and returned a filtered image. In order to optimize this algorithm, both the center frequency and bandwidth had to be optimized. Figure 3 shows this optimization for OCT and micro-CT, where arrays of images are shown, with the center frequency increasing in the columns from left-to-right, and the bandwidth increasing in the rows, from top-to-bottom. For both OCT and micro-CT images, the spatial frequency filter was able to isolate the tumor area. The spatial frequencies were determined by multiplying the number of pixels by the frequency variable and dividing by the size of the image in millimeters. This segmentation algorithm required 0.95 s per OCT image and 1.8 s per micro-CT image.

The third segmentation method used a texture-based algorithm, because the entropy and texture of tumor and adipose regions should be different. This approach was optimized around the variables of kernel size and correlation distance as seen in Fig. 4. This method yielded the best qualitative results for processing OCT images, because it was able to clearly isolate the tumor region. However, the parameters were highly sensitive to specific images and needed to be optimized for each image, often giving erroneous results if not recalibrated for each image. Furthermore, when applied to micro-CT images, this algorithm had difficulty in distinguishing the borders of tumor regions, because the texture of the micro-CT images was universally grainy. The $n1$ variable identified in Fig. 4 is the width and height of the kernel size, increasing from top-to-bottom. The $n2$ variable is the square of the correlation distance, increasing from left-to-right. This algorithm required 2.3 s per OCT image and 2.3 s per micro-CT image.

To validate our selection of the given threshold values, we varied these threshold values slightly and re-analyzed the images in the study set to determine the effect that slight variations in the thresholds would have on the measured outcomes. Few differences were noted for the intensity and spatial filters, validating the choice of thresholds for these filters. However, more variability was noted for the texture-based filter, as noted above, indicating that the use of this filter approach would likely be more tissue specific.

3.3. *Automated segmentation*

Following the optimization of these algorithm parameters based on visual inspection of segmentation outcomes compared to the original OCT and micro-CT images, automated segmentation of the larger image datasets were performed. In order to determine the effectiveness of each segmentation algorithm, a training set was performed with $n = 25$ OCT and $n = 25$ micro-CT images, comparing the area and perimeter of the segmented areas to a gold-standard of visual segmentation. Figure 5 shows the comparison of segmented areas for each method, after being normalized by the area determined by visual segmentation. Only the spatial frequency filter applied to the micro-CT images was shown to be statistically similar ($p > 0.05$) to the area segmented by visual inspection, and it was shown to be the closest to the visual segmentation of tumor area in OCT as well. Subsequently, the spatial frequency algorithm was used in the automated portion of this study as the normalizing quantity. The intensity-based filter segmented a much larger area than visual segmentation because it did not accurately account for noise in the images. The texture-based filter was not able to segment a tumor area approximately 25% of the time, and also had limitations with the micro-CT images, resulting in large error bars and smaller segmented areas. This is likely due to the highly variable texture within the images, from the high heterogeneity of the tissue types.

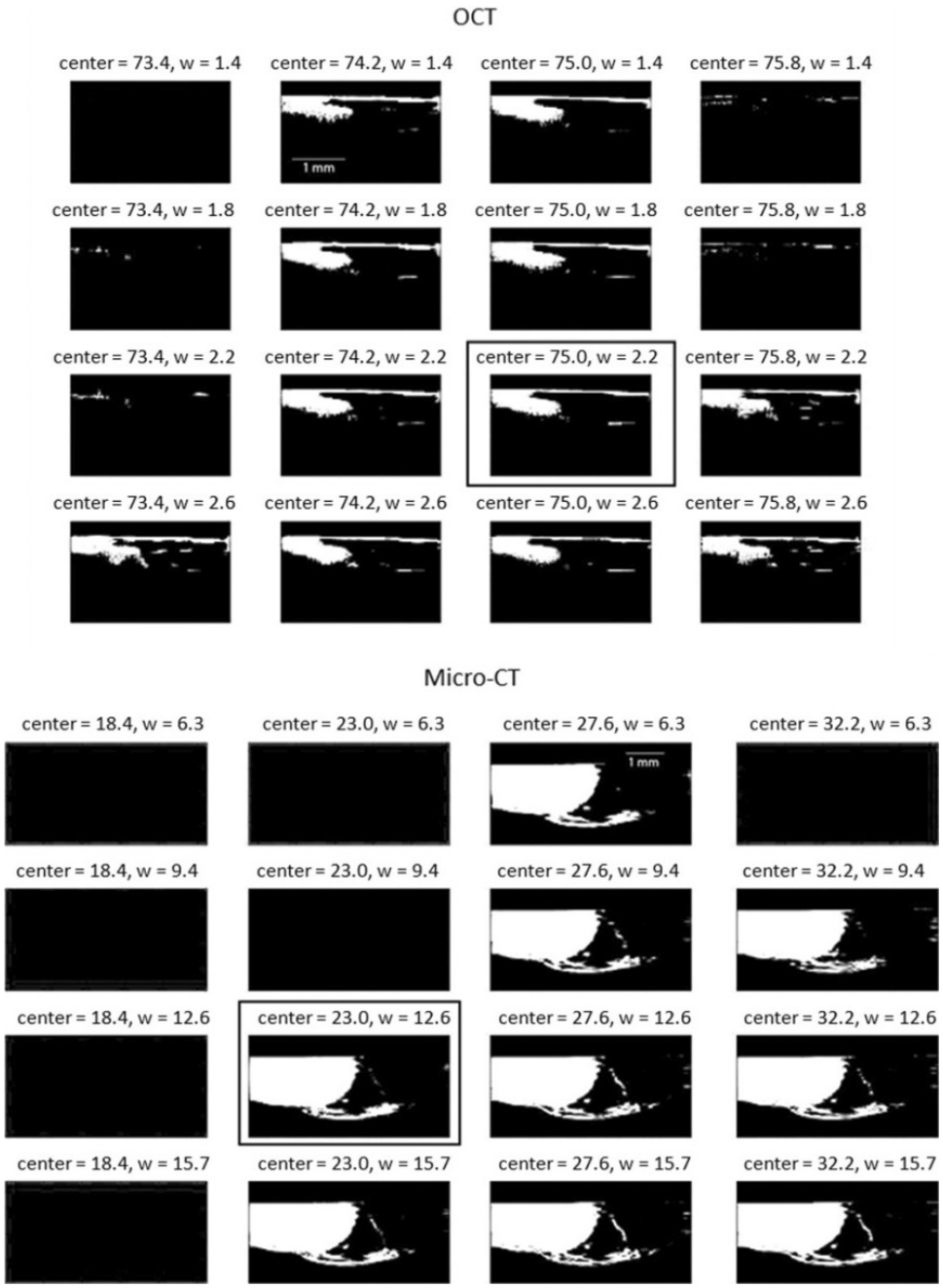

Fig. 3. Optimization of spatial frequency filtering. In both sets of OCT and micro-CT images, the tumor tissue is located on the left. The center spatial frequencies vary in the range of 73.4−75.8 cycles/mm from left-to-right for OCT and 18.4−32.2 cycles/mm from left-to-right for micro-CT. The bandwidth varies in the range 1.4−2.6 cycles/mm from top-to-bottom for OCT and 6.3−15.7 cycles/mm from top-to-bottom for micro-CT. The optimal set of parameters has a center spatial frequency of 74.9 cycles/mm and a bandwidth of 2.2 cycles/mm for OCT, and a center spatial frequency of 23.01 cycles/mm and a bandwidth of 12.3 cycles/mm for micro-CT (boxes).

Additionally, the perimeter of automatically segmented areas was compared to visually segmented areas (see Fig. 6). The perimeter of the tumor regions in the OCT images segmented with the intensity method was large because many small areas were isolated, each contributing to the perimeter measurement. For the spatial frequency algorithm, the perimeter was also larger than by visual segmentation because there was more detail in choosing the boundaries of the area. Finally, the

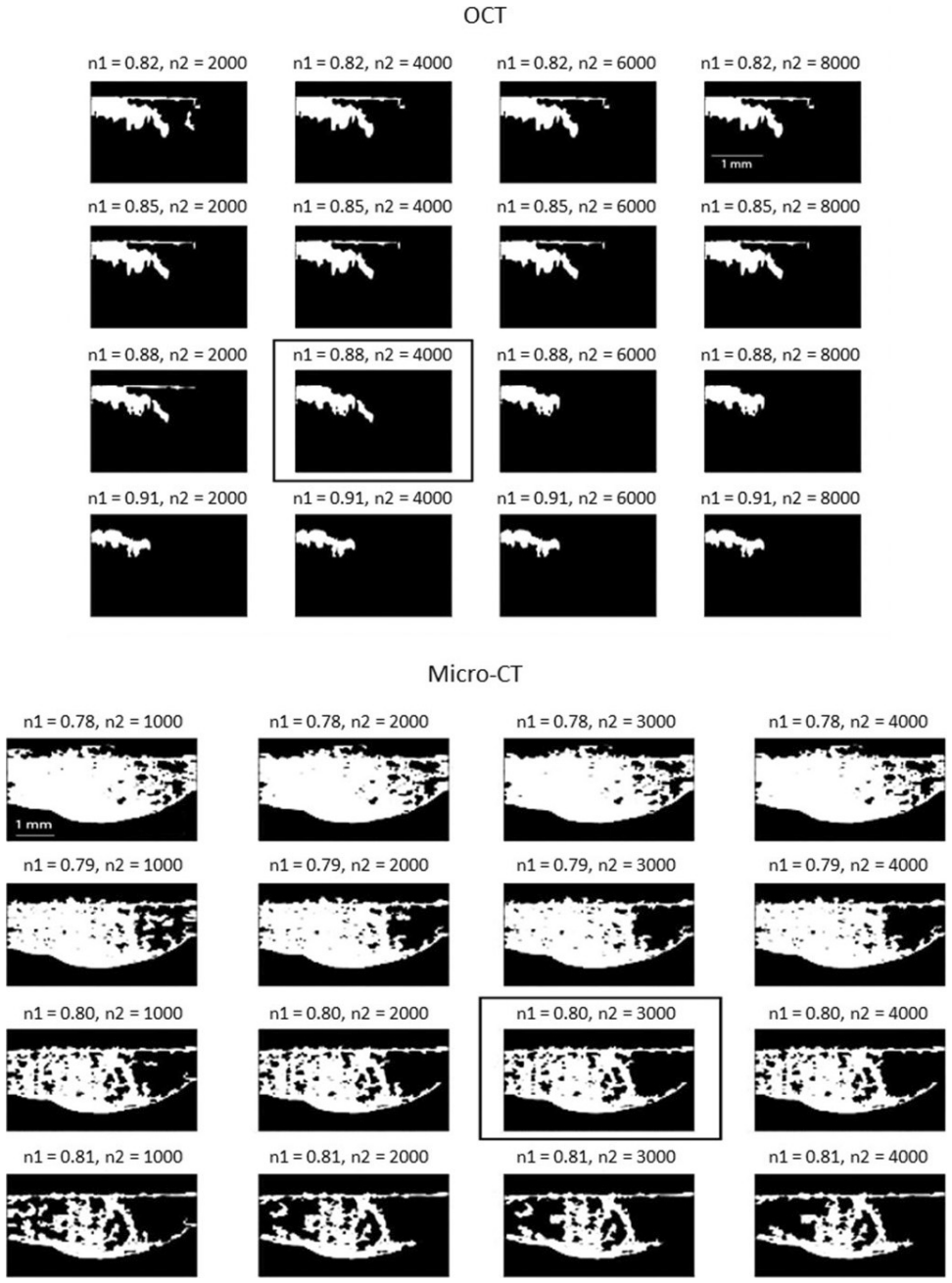

Fig. 4. Optimization of texture-based filtering. In both sets of OCT and micro-CT images, the tumor tissue is located on the left. The columns show increasing correlation distance ($n2$) from left-to-right and the rows show increasing kernel size ($n1$) from top-to-bottom. The optimum configurations are selected visually (boxes).

texture-based method was closest to visual inspection because the algorithm forms one continuous region based on similar texture characteristics.

Finally, based on the findings from the training set, these algorithms were applied to the remainder of the datasets, including images where tumor regions were larger and smaller. In each of these images, the intensity and texture-based algorithms were normalized to the areas found by the spatial frequency filter. This was done because the spatial frequency algorithm was closest to visual segmentation in the training set (see Fig. 5). In Fig. 7, it can be seen that intensity-based segmentation consistently found larger areas than those identified by the spatial frequency algorithm, as shown earlier. However, the texture-based method performed better

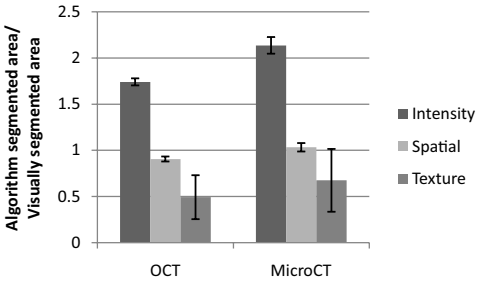

	Intensity	Spatial	Texture
OCT	1.88E-10	0.00012	2.24E-06
Micro-CT	1.38E-08	0.094259	2.20E-05

Fig. 5. Average area of tumor found by each segmentation method, normalized to visual segmentation (training dataset, $n = 25$) with error bars representing standard deviation. A Student's t-test comparing the mean of areas found by each method with the mean obtained by visual inspection was performed. The p-values are shown in the table. Note, because the data is normalized, areas closer to 1 more closely approach the area determined by visual segmentation.

for OCT than micro-CT. This is consistent with previous findings, but the texture-based method has the additional advantage of finding smaller numbers of isolated areas.

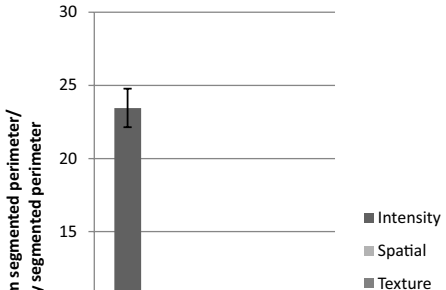

	Intensity	Spatial	Texture
OCT	5.06E-34	2.10E-32	1.31E-3
Micro-CT	3.48E-16	1.06E-05	2.68E-16

Fig. 6. Average perimeter of tumor found by each method normalized to visual segmentation (training dataset, $n = 25$) with error bars representing standard deviation. A Student's t-test comparing the mean of perimeters found by each method with the perimeter obtained by visual inspection was performed. The p-values are shown in the table. Note, because the data is normalized, perimeters closer to 1 more closely approach the perimeter determined by visual segmentation.

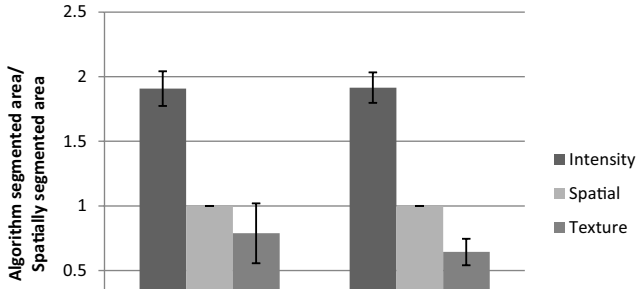

	Intensity	Texture
OCT	1.50E-170	1.12E-49
Micro-CT	2.45E-95	6.96E-26

Fig. 7. Comparison of automatic segmentation algorithms. Areas of tumor segmented by each algorithm are normalized to areas from the spatial frequency algorithm ($n = 1250$ for OCT, $n = 760$ for micro-CT), with error bars representing standard deviation. A Student's t-test comparing the means of the areas found by each method with the area obtained by the spatial frequency filter was performed. The p-values are shown in the table.

In the future, algorithms can be developed to automatically determine and evaluate threshold settings based on specific breast cancer sub-types and image features. Also, a combination of segmentation and filter methods may be useful for automatically identifying areas of tumor so that real-time segmentation of OCT can be used in the operating room without the need for operator training to read and interpret the OCT images. Additionally, these algorithms can be expanded to segment 3D datasets to isolate 3D volumes of tumors.

4. Conclusions

Intraoperative OCT has been shown to identify positive tumor margins during breast cancer surgery. Because X-ray mammography and specimen radiography are typically used in the screening, diagnosis and treatment of breast cancer, this study sought to segment, co-register and correlate image-based findings of breast cancer observed with OCT and X-ray imaging (micro-CT). This multi-modal (and multi-scale) imaging approach has the benefit of leveraging the large volume of image data acquired using X-ray imaging, and relating this information to

the high-resolution real-time OCT. Future work will extend the findings of this study to intraoperative OCT, from either resected tumor specimens or even *in vivo* within the tumor cavity.

This study compared the effectiveness of three algorithms for automatically segmenting OCT and micro-CT images of human breast tissue and tumors. These algorithms were based on intensity, spatial frequency and texture-based segmentation approaches. The spatial frequency algorithm had the most consistent segmentation of tumor areas. However, the intensity and texture-based algorithms each had advantages that could be incorporated into a more sophisticated segmentation algorithm in the future. Quantitatively determining the ability to segment and co-register images between OCT and X-ray imaging, and automating the registration process, will offer the potential to more comprehensively evaluate tissue for diagnostic purposes.

Acknowledgment

We thank Darold Spillman from the Beckman Institute for Advanced Science and Technology on the campus of the University of Illinois at Urbana-Champaign for his assistance with logistical and information technology support. This research was supported in part by a grant from the U.S. National Institutes of Health, R01 EB012479 (S.A.B.). Jonathan Sun was also supported by a Carver Foundation Graduate Fellowship. Additional information can be obtained at http://biophotonics.illinois.edu.

References

1. American Cancer Society, Cancer Facts & Figures 2013, American Cancer Society, Atlanta (2013).
2. J. Chhatwal, O. Alagoz, E. S. Burnside, "Optimal breast biopsy decision-making based on mammographic features and demographic factors," *Oper. Res.* **58**, 1577−1591 (2010).
3. D. G. Fryback, N. K. Stout, M. A. Rosenberg, A. Trentham-Dietz, V. Kuruchittham, P. L. Remington, "The Wisconsin breast cancer epidemiology simulation model," *J. National Cancer Inst. Monogr.* **36**, 37−47 (2006).
4. R. T. Greenlee, T. Murray, S. Bolden, P. A. Wingo, "Cancer statistics," *CA Cancer J. Clin.* **50**, 7−33 (2000).
5. D. Huang, E. A. Swanson, C. P. Lin, J. S. Schuman, W. G. Stinson, W. Chang, M. R. Hee, T. Flotte, K. Gregory, C. A. Puliafito, J. G. Fujimoto, "Optical coherence tomography," *Science* **254**, 1178−1181 (1991).
6. *Handbook of Optical Coherence Tomography*, B. E. Bouma, G. J. Tearney, Eds., Marcel Dekker, Inc. (2002).
7. *Optical Coherence Tomography: Technology and Applications*, W. Drexler, J. G. Fujimoto, Eds., Springer (2008).
8. F. G. Holz, R. F. Spaide, *Medical Retina: Focus on Retinal Imaging*, Springer (2010).
9. V. J. Srinivasan, B. K. Monson, M. Wojtkowski, R. A. Bilonick, I. Gorczynska, R. Chen, J. S. Duker, J. S. Schuman, J. G. Fujimoto, "Characterization of outer retinal morphology with high-speed, ultrahigh-resolution optical coherence tomography," *Invest. Ophthalmol. Vis. Sci.* **49**, 1571−1579 (2008).
10. M. C. Lim, S. T. Hoh, P. J. Foster, T. H. Lim, S. J. Chew, S. K. Seah, T. Aung, "Use of optical coherence tomography to assess variations in macular retinal thickness in myopia," *Invest. Ophthalmol. Vis. Sci.* **46**, 974−978 (2005).
11. C. A. Toth, D. G. Narayan, S. A. Boppart, M. R. Hee, J. G. Fujimoto, R. Birngruber, C. P. Cain, C. D. DiCarlo, W. P. Roach, "A comparison of retinal morphology viewed by optical coherence tomography and by light microscopy," *Arch. Ophthalmol.* **115**, 1425−1428 (1997).
12. A. Mistlberger, J. M. Liebmann, D. S. Greenfield, M. E. Pons, S. T. Hoh, H. Ishikawa, R. Ritch, "Heidelberg retina tomography and optical coherence tomography in normal, ocular-hypertensive, and glaucomatous eyes," *Ophthalmology* **106**, 2027−2032 (1999).
13. T. H. Ko, J. G. Fujimoto, J. S. Duker, L. A. Paunescu, W. Drexler, C. R. Baumal, C. A. Puliafito, E. Reichel, A. H. Rogers, J. S. Schuman, "Comparison of ultrahigh- and standard-resolution optical coherence tomography for imaging macular hole pathology and repair," *Ophthalmology* **111**, 2033−2043 (2004).
14. R. J. Linnola, O. Findl, B. Hermann, H. Sattmann, A. Unterhuber, R. P. Happonen, W. Drexler, "Intraocular lens-capsular bag imaging with ultrahigh-resolution optical coherence tomography pseudophakic human autopsy eyes," *J. Cataract Refract. Surg.* **31**, 818−823 (2005).
15. L. L. Otis, M. J. Everett, U. S. Sathyam, B. W. Colston, Jr., "Optical coherence tomography: A new imaging technology for dentistry," *J. Am. Dent. Assoc.* **131**, 511−514 (2000).
16. L. L. Otis, B. W. Colston, Jr., M. J. Everett, H. Nathel, "Dental optical coherence tomography:

A comparison of two *in vitro* systems," *Dentomaxillofac. Radiol.* **29**, 85−89 (2000).
17. B. W. Colston, Jr., M. J. Everett, U. S. Sathyam, L. B. DaSilva, L. L. Otis, "Imaging of the oral cavity using optical coherence tomography," *Monogr. Oral Sci.* **17**, 32−55 (2000).
18. D. Fried, J. Xie, S. Shafi, J. D. Featherstone, T. M. Breunig, C. Le, "Imaging caries lesions and lesion progression with polarization sensitive optical coherence tomography," *J. Biomed. Opt.* **7**, 618−627 (2002).
19. M. C. Pierce, J. Strasswimmer, B. H. Park, B. Cense, J. F. de Boer, "Advances in optical coherence tomography imaging for dermatology," *J. Invest. Dermatol.* **123**, 458−463 (2004).
20. J. Welzel, "Optical coherence tomography in dermatology: A review," *Skin Res. Technol.* **7**, 1−9 (2001).
21. J. Welzel, E. Lankenau, R. Birngruber, R. Engelhardt, "Optical coherence tomography of the human skin," *J. Am. Acad. Dermatol.* **37**, 958−963 (1997).
22. S. A. Boppart, W. Luo, D. L. Marks, K. W. Singletary, "Optical coherence tomography: Feasibility for basic research and image-guided surgery of breast cancer," *Breast Cancer Res. Treat.* **84**, 85−97 (2004).
23. P. L. Hsiung, D. R. Phatak, Y. Chen, A. D. Aguirre, J. G. Fujimoto, J. L. Connolly, "Benign and malignant lesions in the human breast depicted with ultrahigh resolution and three-dimensional optical coherence tomography," *Radiology* **244**, 865−874 (2007).
24. F. T. Nguyen, A. M. Zysk, E. J. Chaney, J. G. Kotynek, U. J. Oliphant, F. J. Bellafiore, K. M. Rowland, P. A. Johnson, S. A. Boppart, "Intraoperative evaluation of breast tumor margins with optical coherence tomography," *Cancer Res.* **69**, 8790−8796 (2009).
25. W. Luo, F. T. Nguyen, A. M. Zysk, T. S. Ralston, J. Brockenbrough, D. L. Marks, A. L. Oldenburg, S. A. Boppart, "Optical biopsy of lymph node morphology using optical coherence tomography," *Technol. Cancer Res. Treat.* **4**, 539−547 (2005).
26. F. T. Nguyen, A. M. Zysk, E. J. Chaney, S. G. Adie, J. G. Kotynek, U. J. Oliphant, F. J. Bellafiore, K. M. Rowland, P. A. Johnson, S. A. Boppart, "Optical coherence tomography: The intraoperative assessment of lymph nodes in breast cancer," *IEEE Eng. Med. Biol. Mag.* **29**, 63−70 (2010).
27. R. John, S. G. Adie, E. J. Chaney, M. Marjanovic, K. V. Tangella, S. A. Boppart, "Three-dimensional optical coherence tomography for optical biopsy of lymph nodes and assessment of metastatic disease," *Ann. Surg. Oncol.* DOI: 10.1245/s10434-012-2434-z (2012).
28. T. S. Ralston, D. L. Marks, P. S. Carney, S. A. Boppart, "Interferometric synthetic aperture microscopy," *Nat. Phys.* **3**, 129−134 (2007).
29. L. K. Jacobs, P. S. Carney, A. J. Cittadine, D. T. McCormick, A. L. Somera, D. A. Darga, J. L. Putney, S. G. Adie, P. Ray, K. A. Cradock, L. Tafra, E. W. Gabrielson, S. A. Boppart, "Intraoperative assessment of tumor margins with a new optical imaging technology: A multi-center, randomized, blinded clinical trial," *Proc. CTRC-AACR Breast Cancer Symp.*, San Antonio, TX, December 4−8 (2012).
30. I. J. Bigio, S. G. Bown, G. Briggs, C. Kelley, S. Lakhani, D. Pickard, P. M. Ripley, I. G. Rose, C. Saunders, "Diagnosis of breast cancer using elastic-scattering spectroscopy: Preliminary clinical results," *J. Biomed. Opt.* **5**, 221−228 (2000).
31. A. S. Haka, Z. Volynskaya, J. A. Gardecki, J. Nazemi, J. Lyons, D. Hicks, M. Fitzmaurice, R. R. Dasari, J. P. Crowe, M. S. Feld, "*In vivo* margin assessment during partial mastectomy breast surgery using Raman spectroscopy," *Cancer Res.* **66**, 3317−3322 (2006).
32. L. Xi, S. R. Grobmyer, L. Wu, R. Chen, G. Zhou, L. G. Gutwein, J. Sun, W. Liao, Q. Zhou, H. Xie, H. Jiang, "Evaluation of breast tumor margins *in vivo* with intraoperative photoacoustic imaging," *Opt. Express* **20**, 8726−8731 (2012).
33. S. Kennedy, J. Geradts, T. Bydlon, J. Q. Brown, J. Gallagher, M. Junker, W. Barry, N. Ramanujam, L. Wilke, "Optical breast cancer margin assessment: An observational study of the effects of tissue heterogeneity on optical contrast," *Breast Cancer Res.* **12**, R91 (2010).
34. Available at http://www.mathworks.com/help/images/functionlist.html, MATLAB, Mathworks, Inc.